Current Optics and Photonics
Vol. 4, No. 4, August 2020, pp. 373-379

ISSN: 2508-7266(Print) / ISSN: 2508-7274(Online)
DOI: https://doi.org/10.3807/COPP.2020.4.4.373

Terahertz Generation by a Resonant Photoconductive Antenna

Kanghee Lee[1,2], Seong Cheol Lee[1], Won Tae Kim[1], Jagang Park[2], Bumki Min[2], and Fabian Rotermund[1]*

[1]*Department of Physics, Korea Advanced Institute of Science and Technology (KAIST), Daejeon 34141, Korea*
[2]*Department of Mechanical Engineering, Korea Advanced Institute of Science and Technology (KAIST), Daejeon 34141, Korea*

(Received April 14, 2020 : revised May 20, 2020 : accepted May 26, 2020)

In this study, we investigate terahertz (THz) generation by a photoconductive antenna with electrodes in the shape of split-ring resonators. According to our theoretical investigation based on a lumped-circuit model, the inductance of this electrode structure leads to resonant behavior of the photo-induced current. Hence, near the resonance frequency the spectral components generated by a resonant photoconductive antenna can be greater than those produced by a non-resonant one. For experimental verification, a resonant photoconductive antenna, which possesses a resonance mode at 0.6 THz, and a non-resonant photoconductive antenna with stripe-shaped electrodes were fabricated on a semi-insulating GaAs substrate. The THz generation by both of the photoconductive antennas demonstrated a good agreement with the theoretically expected results. The observed relationship between the resonant electrodes of the photoconductive antenna and the generated THz spectrum can be further employed to design a narrow-band THz source with an on-demand frequency.

Keywords : Ultrafast optics, Terahertz optics, Photoconductive antenna, Split-ring resonator
OCIS codes : (320.7080) Ultrafast devices; (300.6495) Spectroscopy, terahertz; (160.5140) Photoconductive materials; (160.3918) Metamaterials

I. INTRODUCTION

Electromagnetic waves in the terahertz (THz) frequency range, located between the microwave and infrared frequency ranges, are expected to be essential for future applications in electronics and optics, such as wireless communication [1, 2] and ultrafast motion tracking of molecules [3]. Advances in ultrafast laser technologies provide THz waves at the laboratory level, and a photoconductive antenna (PCA) is representative of the devices for THz generation in ultrafast laser systems [4]. In the process of THz generation by a PCA, an abrupt current flow is induced between its cathode and anode by ultrafast optical excitation on a semiconductor substrate, such as semi-insulating GaAs or low-temperature-grown GaAs. This abrupt variation in the photo-induced current becomes a radiation source of THz electromagnetic waves, as described by the following equation [4]:

$$E_{THz}(t) \propto \frac{dI(t)}{dt}, \tag{1}$$

where $E_{THz}(t)$ and $I(t)$ represent the generated THz field and photo-induced current, respectively. Thus, manipulating the temporal variation of the photo-induced current, i.e., $\frac{dI(t)}{dt}$, is the key to generating THz waves. Based on this principle, to expand the utility of PCAs, their THz generation has been studied by various approaches, such as selecting different substrate materials [5-7] or coupling with an optical nanoantenna [8, 9]. Similarly, the dependence of THz generation on the electrode structures of PCAs has

*Corresponding author: rotermund@kaist.ac.kr, ORCID 0000-0001-9053-3916
Color versions of one or more of the figures in this paper are available online.

also been extensively studied [10-13]. In particular, the spectral features of the THz generation by meta-atom-loaded PCAs and its optical modulation have been investigated [13]. However, the relation between the generated THz waves and the resonant electrode structures has not been studied explicitly, to the best of our knowledge.

In this study, we theoretically and experimentally explore the THz generation by a resonant PCA (RPCA), in which the interdigitated electrodes are fabricated as arrays of split-ring resonators (SRRs) on a semi-insulating GaAs substrate. Owing to the inductance of such shaped electrodes, the RPCA has a resonant mode ω_0 at 0.6 THz. The spectrum of the THz waves generated from the RPCA is also strongly related to the resonance, and THz waves with enhanced spectral components can be generated by the RPCA, compared to that by a non-resonant PCA (NRPCA).

II. DETAILS OF FABRICATED PCAS

Figure 1 displays the two PCAs that are fabricated with interdigitated-type electrodes on semi-insulating GaAs substrates. The NRPCA (Fig. 1(a)) has stripe-shaped electrodes, which are extensively used in PCAs [14, 15], whereas the RPCA (Fig. 1(b)) has electrodes shaped as arrays of SRRs. We choose a lattice constant of 81 μm, electrode width of 5 μm and gap width of 4 μm for the RPCA. These array-type large-area electrodes are initially patterned to apply bias fields in two spatially alternating directions. Subsequently, a mask layer, vertically isolated from the electrodes by a polyimide layer with a thickness of 1 μm, is fabricated to generate photo-carriers only in the regions where the bias field is applied in the same direction, similar to previous studies of PCAs with interdigitated-type electrodes [14, 15]. All metal structures of the PCAs are patterned on 150-nm-thick gold with a 10-nm-thick chromium adhesion layer.

The resonant behaviors of the electrodes of both the NRPCA and RPCA can be directly identified by THz transmission measurements. Because the impedance from the inductance of the electrodes of the NRPCA is negligible in the measured frequency range, the transmission from the NRPCA does not exhibit resonant behavior, as shown in Fig. 1(c). In contrast, in the transmission from the RPCA a resonance peak appears at approximately 0.6 THz (as presented in Fig. 1(d)) because of the substantial inductance of its SRRs. The resonance frequency ω_0 is determined by the capacitance C and inductance L of the SRRs of the RPCA as $\omega_0 = 1/\sqrt{CL}$.

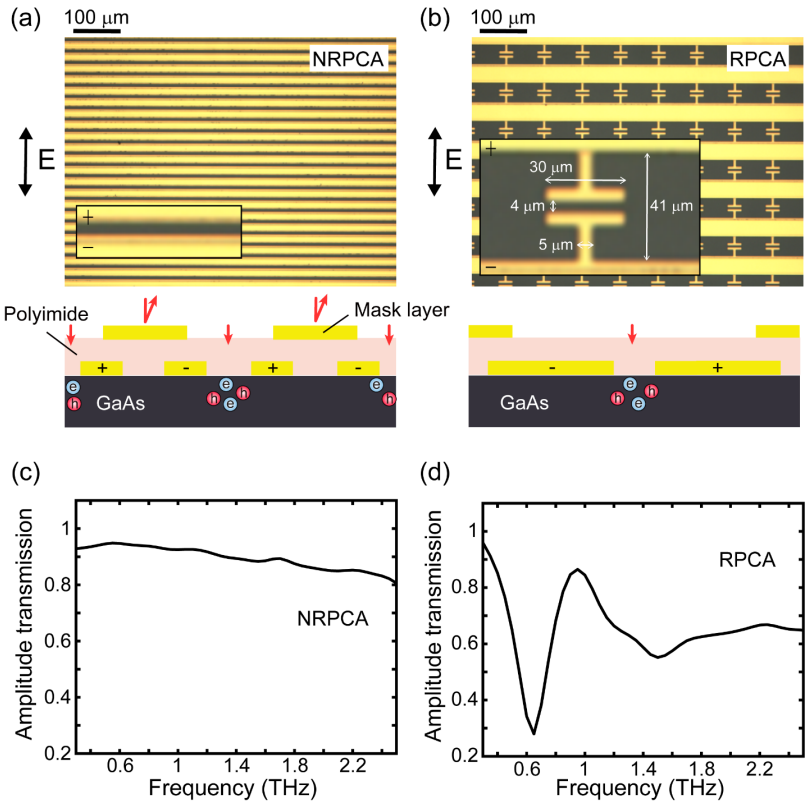

FIG. 1. (a) Microscopic images of the NRPCA (top panel) and schematic of its cross-section (bottom). The inset in the top panel presents an enlarged view. The bidirectional arrow indicates the THz field direction for the transmission measurement in (c). (b) Microscopic images of the RPCA (top panel) and schematic of its cross section (bottom). (c) Measured amplitude transmission from the NRPCA. (d) Measured amplitude transmission from the RPCA.

III. THEORY

The temporal evolution of the photo-induced current in PCAs can be theoretically understood using a lumped circuit model. For PCAs with no inductance, a photo-induced resistor $r(t)$ and a capacitor C connected in parallel are typically used to explain the photo-induced current dynamics [16, 17], as depicted in Fig. 2(a). For our PCAs, C can be regarded as a constant because the dimension of the electrode structure is much larger than that of the photo-excited region. Then, using Kirchhoff's circuit laws it can be easily derived that the photo-induced current I_{tot} is determined instantaneously as $V/r(t)$. In our calculation, we assume that $r(t)$ does not change after the optical excitation, because the lifetime of a photo-induced carrier in GaAs is significantly longer than a few pico-seconds [18]. In addition, we assume that the pulse width of an ultrafast laser pulse is infinitesimally short; therefore, $r(t)$ changes instantaneously from infinity to a certain resistance R as follows:

$$r(t)=\begin{cases}\infty\,(t<0)\\ R(t\geq 0)\end{cases}, \tag{2}$$

where $t=0$ indicates the time of optical excitation. Thus, the temporal evolution of the photo-induced currents in this circuit can also be treated as a step function, and according to Eq. (1) the electromagnetic radiation from a current with such step-like variation can be treated as a Dirac-delta function. It is noteworthy that the Coulomb screening also affects both the photo-induced current dynamics and the THz radiation [19-21]; however, for simplicity, we do not consider Coulomb screening here.

An RPCA with a substantial inductance L can be modeled as a circuit with an additional inductor, as illustrated in Fig. 2(b), and the photo-induced current dynamics are now determined by both the inductance L and the capacitance C. From Kirchhoff's circuit laws, the relations between the current through the resistor, I_1, and that through the capacitor, I_2, can be derived as follows:

$$I_1+I_2=I_{tot}, \tag{3a}$$

$$\frac{Q_2}{C}=r(t)I_1, \tag{3b}$$

$$\frac{Q_2}{C}+L\frac{dI_{tot}}{dt}=V, \tag{3c}$$

where I_{tot}, Q_2, and V are the total current through the circuit, charge in the capacitor, and applied voltage, respectively. Solving these equations for $t\geq 0$ $(r(t)=R)$ and using $I_2=\frac{dQ_2}{dt}$, the dynamical equation for Q_2 is derived as follows:

$$\frac{Q_2}{C}+\frac{L}{RC}\frac{dQ_2}{dt}+L\frac{d^2Q_2}{dt^2}=V. \tag{4}$$

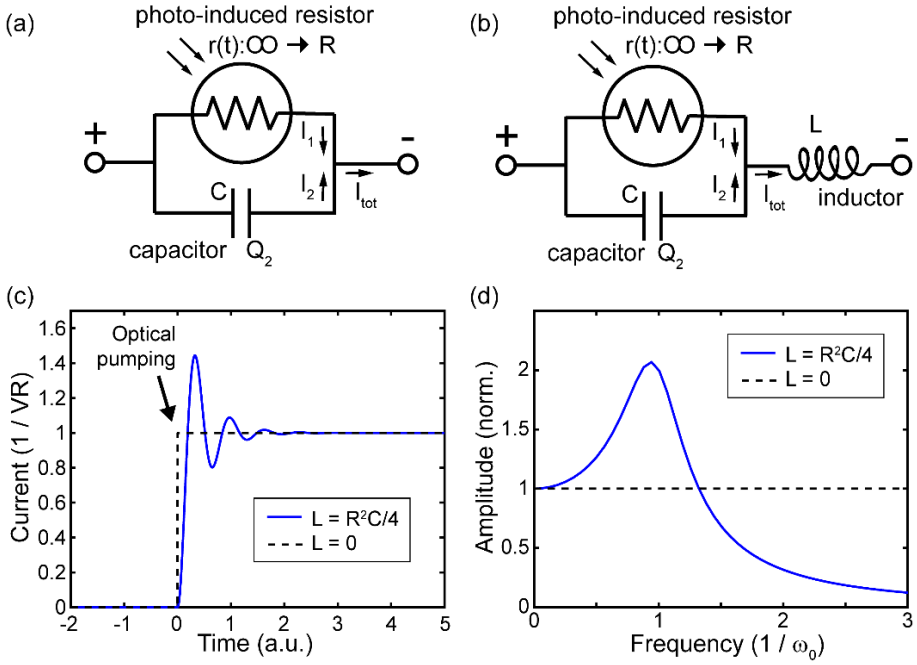

FIG. 2. (a) Lumped circuit for the NRPCA. (b) Lumped circuit for the RPCA. (c) Temporal evolution of the photo-induced current in a PCA with an inductor (blue solid line) and without an inductor (black dashed line). (d) Spectra of the radiating fields from a PCA with an inductor (blue solid line) and without an inductor (black dashed line).

Before the ultrafast laser pulse is incident upon the RPCA, there is no current flow ($I_{tot}=0$) and the charge is stored in the capacitor as $Q_2=CV$. Adopting these conditions as the initial conditions of the photo-current dynamics, the temporal evolution of I_{tot} can be calculated from Eq. (4). The calculated result for I_{tot} with inductance $L=R^2C/4$ and capacitance $C=2/\omega_0 R$ and that with no inductance, i.e., $L=0$, are represented in Fig. 2(c) as a blue line and a black dashed line respectively. Note that the values for L and C are selected to fit the ratio of the measured spectral amplitudes near the resonance frequency (Fig. 4(e)). As presented in Fig. 2(c), an oscillation arises around the equilibrium point V/R in the temporal evolution of the photo-induced current for the circuit with inductance. Consequently, the radiated spectrum for this circuit is significantly different from that for the circuit without inductance, as displayed in Fig. 2(d). In particular, the spectral components near ω_0 are enhanced by the inductance, whereas those significantly beyond ω_0 are reduced. It is worth noting that the radiated spectrum from the NRPCA is constant, due to the sudden time variation of the photo-induced current from laser pulse width that is assumed to be infinitesimally short. In a real experiment, the spectrum is limited by the pulse width of the pump beam.

IV. EXPERIMENTAL PROCEDURE

To confirm our theoretical expectation, the THz generation from both PCAs is measured by conventional THz time-domain spectroscopy (THz-TDS), as illustrated in Fig. 3. A homemade Ti:sapphire laser oscillator is used for the THz-TDS, and its repetition rate, center wavelength, and pulse width are 90 MHz, 800 nm and 50 fs, respectively. A horizontally polarized ultrafast laser beam, the electric field of which is perpendicular to the bias field, is incident upon the PCA surface. A bias voltage of 5 V is applied to the PCA for the THz generation. To transfer the THz waves to the detection part, we use two off-axis parabolic mirrors with focal lengths of 50 mm and 100 mm, respectively. A lens with a focal length of 25 mm is used to inject the laser pulse onto the PCA, and the spot size of the ultrafast laser beam is adjusted by controlling the displacement between the lens and the PCA. Knife-edge scanning is employed to measure the spot size before the THz-generation experiment. The generated THz waves with a field direction parallel to the bias field are detected by a well-known electro-optic sampling technique, using a ZnTe crystal with a thickness of 1 mm [4].

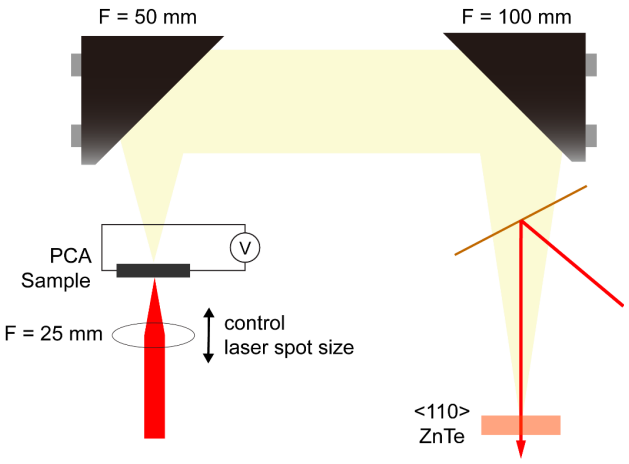

FIG. 3. Schematic diagram of the experimental setup.

V. EXPERIMENTAL RESULTS

To realize the connected-in-parallel photo-induced resistor and capacitor, as in Figs. 2(a) and 2(b), only the gap region of the PCA should be optically excited. To accurately align the laser pumping onto the gap region of the PCA, particularly onto that of the SRRs in the RPCA, we initially perform laser THz emission microscopy (LTEM) [22, 23] for the PCAs using a laser spot size of 20 μm in diameter. Because the THz generation strongly depends on the relative position of this small laser spot on the electrode structure, and is maximized when the laser spot is located at the electrode gap, the position of the laser spot can be directly determined by the LTEM measurement. The power of the ultrafast laser beam is adjusted to be 30 mW for the measurement. The field amplitudes of the generated THz waves are measured by two-dimensional raster scanning of the PCA at the peak positions of the THz waves, and as displayed in the corresponding microscopic images (Figs. 4(a) and 4(b)), the field amplitudes are maximized when the laser spot is aligned onto the gap region of the PCA.

We then measure the full time traces of the generated THz waves at the signals' maximum positions, indicated by arrows in Figs. 4(a) and 4(b), to verify the theoretical expectation of spectral enhancement near the resonance frequency. The THz fields generated by the RPCA (Fig. 4(c)) and NRPCA (Fig. 4(d)) present similar peak field amplitudes in the time domain; however, the field profile generated by the RPCA has a longer cycle than that from the NRPCA. In the frequency domain (Fig. 4(e)), the THz waves from the RPCA have larger spectral amplitudes near the resonance frequency than those from the NRPCA. In contrast, the number of spectral components significantly beyond the resonance frequency generated by the RPCA is less than that from the NRPCA. This observed spectral difference in the THz waves generated by the two PCAs is in excellent agreement with the theoretically expected results, as depicted in Fig. 2(d).

Because the electrodes of the PCAs have array-type structures, we also measure the THz generation for a laser pumping with a spot size larger than the unit cell of the electrode structure. Figure 5 presents the results of THz generation when the PCAs are optically excited with a

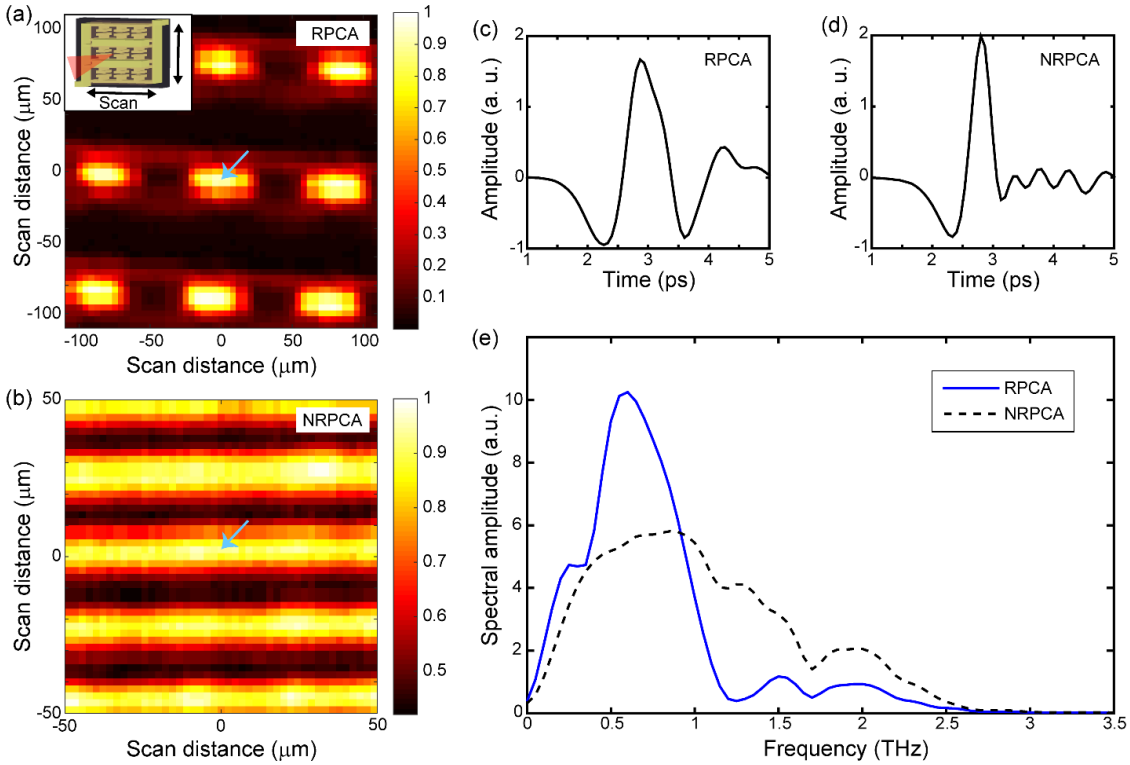

FIG. 4. THz generation with a laser-beam spot size of 20 μm in diameter. (a) LTEM image for the RPCA. The arrow indicates where the THz field profile is obtained. The inset figure shows a schematic diagram of LTEM imaging. (b) LTEM image for the NRPCA. (c) THz field profile from the RPCA. (d) THz field profile from the NRPCA. (e) Spectra of the generated THz waves from the RPCA (blue solid line) and NRPCA (black dashed line).

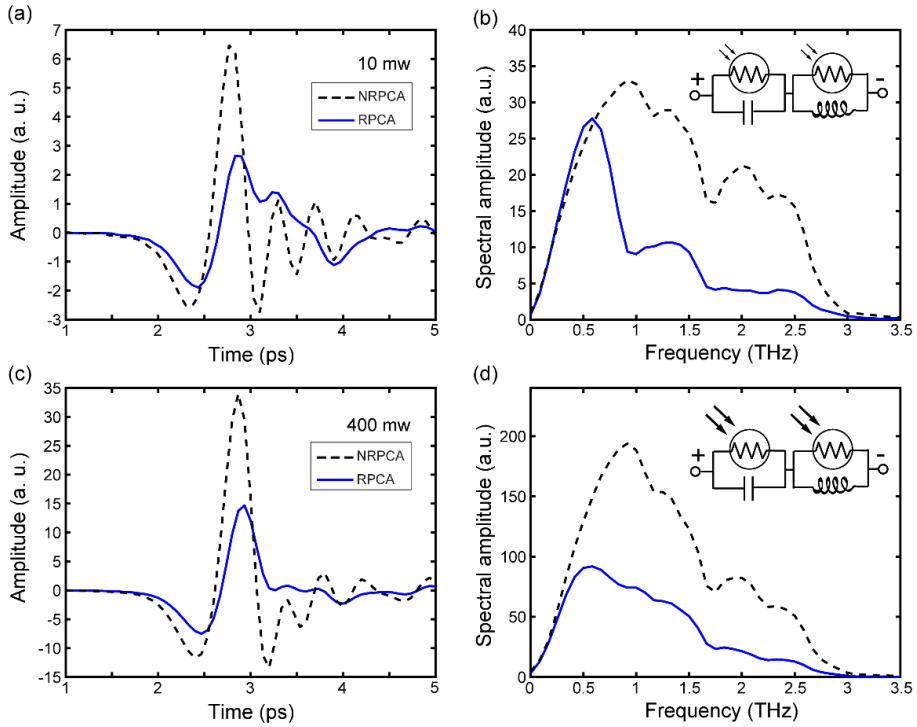

FIG. 5. THz generation with a large beam spot size of 400 μm in diameter. (a, b) Generated THz field profiles (a) from the RPCA (blue solid line) and the NRPCA (black dashed line), and their spectra (b) with a laser pump power of 10 mW. The lumped circuit for the RPCA is also illustrated in (b). (c, d) Generated THz field profiles (c) and their spectra (d) with a laser pump power of 400 mW.

large laser spot size of 400 μm in diameter. This spot size is achieved by displacing the focusing lens slightly backward from the PCA, as illustrated in Fig. 3. Initially we measure the THz generation by each PCA with an optical pumping power of 10 mW. As displayed in the comparison of the THz generation by both PCAs (Figs. 5(a) and 5(b)), the peak field of the generated THz wave from the RPCA is substantially smaller than that from the NRPCA. This is because a significant portion of the laser pumping is injected onto the ring part of the SRRs in the RPCA, instead of onto the gap part. This laser pumping onto the ring part can be interpreted as an additional photo-induced current path, parallel to the inductor of the circuit (inset in Fig. 5(b)), that does not affect the overall $\frac{dI(t)}{dt}$ significantly. Moreover, because this additional current path breaks the resonant characteristic of the photo-current dynamics of the RPCA, the generated THz wave from the RPCA with a large laser spot size has a broader spectrum than that with a small spot size (Fig. 4(e)). The broadening of the spectrum is more notable with higher optical pumping power. Because the high laser pumping of 400 mW creates such an additional current path with a much lower resistance, the role of the inductance in the lumped circuit is effectively eliminated, and the resonance peak in the THz spectrum disappears, as displayed in Figs. 5(c) and 5(d). Thus, to generate THz waves with enhanced spectral components from the RPCA by large-area laser excitation, the optical excitation should be ensured to be only onto the gaps of the SRRs, by dividing the laser pump beam appropriately. It is noteworthy that a micro-lens array that suitably aligns the optical pump beam to the gaps of the SRRs may be used for this objective [24].

VI. CONCLUSION

In conclusion, we theoretically and experimentally investigate the THz generation from an RPCA with SRR-shaped electrodes. Compared to the photo-induced current dynamics of an NRPCA with no substantial inductance, those of the RPCA are theoretically expected to exhibit resonance at a certain frequency. Thus, the spectrum of the generated THz waves is also expected to be substantially enhanced near the resonance frequency, compared to that of the THz waves generated from the NRPCA. Our theoretical expectation is in good agreement with the experimental results for THz generation when only the gap part of the RPCA is optically excited. However, when the ring part of the RPCA is optically excited, the inductance is effectively eliminated by an additional current path, and the resonant feature in the measured spectrum disappears.

Because the center frequency of the THz wave generated by a RPCA is closely related to its resonance, narrow-band THz waves with various center frequencies can be generated by modifying the size and design of the RPCA. In addition, the spectral amplitude at such a selectable center frequency can be larger than that from a NRPCA. Thus, the generated THz wave from an appropriately designed RPCA may be utilized as a narrow-band THz source, which has practical applications for target detection in biomedical sensing [25, 26] or security testing [27, 28].

ACKNOWLEDGMENT

K.L., S.C.L., W.T.K, and F.R. acknowledge support from the National Research Foundation of Korea (NRF) through the Korean government (MSIP) (No. 2019R1A2C3003504, 2020R1A4A2002828) and KAERI project. J.P. and B.M. acknowledge support from the NRF through MSIP (Grant Nos. NRF-2017R1A2B3012364) and the Center for Advanced Meta-Materials (CAMM) funded by the Korean Government (MSIP) as a Global Frontier Project (NRF-2014M3A6B3063709). K.L. acknowledges support from the NRF (Grant No. NRF-2019R1A6A3A01091214, 2020R1C1 C1009098).

REFERENCES

1. S. Koenig, D. Lopez-Diaz, J. Antes, F. Boes, R. Henneberger, A. Leuther, A. Tessmann, R. Schmogrow, D. Hillerkuss, R. Palmer, T. Zwick, C. Koos, W. Freude, O. Ambacher, J. Leuthold, and I. Kallfass, "Wireless sub-THz communication system with high data rate," Nat. Photon. **7**, 977-981 (2013).
2. I. F. Akyildiz, J. M. Jornet, and C. Han, "Terahertz band: Next frontier for wireless communications," Phys. Commun. **12**, 16-32 (2014).
3. T. L. Cocker, D. Peller, P. Yu, J. Repp, and R. Huber, "Tracking the ultrafast motion of a single molecule by femtosecond orbital imaging," Nature **539**, 263-267 (2016).
4. Y. S. Lee, *Principles of Terahertz Science and Technology* (Springer, NY, 2009).
5. M. Tani, S. Matsuura, K. Sakai, and S.-I. Nakashima, "Emission characteristics of photoconductive antennas based on low-temperature-grown GaAs and semi-insulating GaAs," Appl. Opt. **36**, 7853-7859 (1997).
6. A. Schwagmann, Z. Y. Zhao, F. Ospald, H. Lu, D. C. Driscoll, M. P. Hanson, A. C. Gossard, and J. H. Smet, "Terahertz emission characteristics of ErAs: InGaAs-based photoconductive antennas excited at 1.55 μm," Appl. Phys. Lett. **96**, 141108 (2010).
7. B. Globisch, R. J. B. Dietz, R. B. Kohlhaas, T. Gobel, M. Schell, D. Alcer, M. Semtsiv, and W. T. Masselink, "Iron doped InGaAs: Competitive THz emitters and detectors fabricated from the same photoconductor," J. Appl. Phys. **121**, 053102 (2017).
8. S.-G. Park, K.-H. Jin, M. Yi, J. C. Ye, J. Ahn, and K.-H. Jeong, "Enhancement of terahertz pulse emission by optical nanoantenna," ACS Nano **6**, 2026-2031 (2012).
9. C. W. Berry, N. Wang, M. R. Hashemi, M. Unlu, and M. Jarrahi, "Significant performance enhancement in photocon-

ductive terahertz optoelectronics by incorporating plasmonic contact electrodes," Nat. Commun. **4**, 1622 (2013).
10. F. Miyamaru, Y. Saito, K. Yamamoto, T. Furuya, S. Nishizawa, and M. Tani, "Dependence of emission of terahertz radiation on geometrical parameters of dipole photoconductive antennas," Appl. Phys. Lett. **96**, 211104 (2010).
11. P. Maraghechi and A. Y. Elezzabi, "Enhanced THz radiation emission from plasmonic complementary Sierpinski fractal emitters," Opt. Express **18**, 27336-27345 (2010).
12. P. Maraghechi and A. Y. Elezzabi, "Experimental confirmation of design techniques for effective bow-tie antenna lengths at THz frequencies," J. Infrared, Millimeter, Terahertz Waves **32**, 897 (2011).
13. K. Takano, Y. Chiyoda, T. Nishida, F. Miyamaru, T. Kawabata, H. Sasaki, M. W. Takeda, and M. Hangyo, "Optical switching of terahertz radiation from meta-atom-loaded photoconductive antennas," Appl. Phys. Lett. **99**, 161114 (2011).
14. A. Dreyhaupt, S. Winnerl, T. Dekorsy, and M. Helm, "High-intensity terahertz radiation from a microstructured large-area photoconductor," Appl. Phys. Lett. **86**, 121114 (2005).
15. P. J. Hale, J. Madeo, C. Chin, S. S. Dhillon, J. Mangeney, J. Tignon, and K. M. Dani, "20 THz broadband generation using semi-insulating GaAs interdigitated photoconductive antennas," Opt. Express **22**, 26358-26364 (2014).
16. D. Auston, "Impulse response of photoconductors in transmission lines," IEEE J. Quantum Electron. **19**, 639-648 (1983).
17. O. A. Castañeda-Uribe, C. A. Criollo, S. Winnerl, M. Helm, and A. Avila, "Comparative study of equivalent circuit models for photoconductive antennas," Opt. Express **26**, 29017-29031 (2018).
18. Y. Shi, Q.-L. Zhou, C. Zhang, and B. Jin, "Ultrafast high-field carrier transport in GaAs measured by femtosecond pump-terahertz probe spectroscopy," Appl. Phys. Lett. **93**, 121115 (2008).
19. J. E. Pedersen, V. G. Lyssenko, J. M. Hvam, P. U. Jepsen, and S. R. Keiding "Ultrafast local field dynamics in photoconductive THz antennas," Appl. Phys. Lett. **62**, 1265-1267 (1993).
20. P. U. Jepsen, R. H. Jacobsen, and S. R. Keiding, "Generation and detection of terahertz pulses from biased semiconductor antennas," J. Opt. Soc. Am. B **13**, 2424-2436 (1996).
21. H. Murakami, S. Fujiwara, I. Kawayama, and M. Tonouchi, "Study of photoexcited-carrier dynamics in GaAs photoconductive switches using dynamic terahertz emission microscopy," Photon. Res. **4**, A9-A15 (2016).
22. T. Kiwa, M. Tonouchi, M. Yamashita, and K. Kawase, "Laser terahertz-emission microscope for inspecting electrical faults in integrated circuits," Opt. Lett. **28**, 2058-2060 (2003).
23. M. Yamashita, K. Kawase, C. Otani, T. Kiwa, and M. Tonouchi, "Imaging of large-scale integrated circuits using laser terahertz emission microscopy," Opt. Express **13**, 115-120 (2005).
24. G. Matthäus, S. Nolte, R. Hohmuth, M. Voitsch, W. Richter, B. Pradarutti, S. Riehemann, G. Notni, and A. Tünnermann, "Microlens coupled interdigital photoconductive switch," Appl. Phys. Lett. **93**, 091110 (2008).
25. D. F. Plusquellic, K. Siegrist, E. J. Heilweil, and O. Esenturk, "Applications of terahertz spectroscopy in biosystems," Chem. Phys. Chem. **8**, 2412-2431 (2007).
26. L. Xie, Y. Yao, and Y. Ying, "The application of terahertz spectroscopy to protein detection: A review," Appl. Spectrosc. Rev. **49**, 448-461 (2014).
27. K. Kawase, Y. Ogawa, Y. Watanabe, and H. Inoue, "Non-destructive terahertz imaging of illicit drugs using spectral fingerprints," Opt. Express **11**, 2549-2554 (2003).
28. J. F. Federici, B. Schulkin, F. Huang, D. Gary, R. Barat, F. Oliveira, and D. Zimdars, "THz imaging and sensing for security applications—explosives, weapons and drugs," Semicond. Sci. Technol. **20**, S266 (2005).